Available online at www.sciencedirect.com

SciVerse ScienceDirect

Acta Materialia 60 (2012) 3849–3860

Acta MATERIALIA

www.elsevier.com/locate/actamat

Densification behavior, microstructure evolution, and wear performance of selective laser melting processed commercially pure titanium

Dongdong Gu [a,b,*], Yves-Christian Hagedorn [b], Wilhelm Meiners [b], Guangbin Meng [a], Rui João Santos Batista [b], Konrad Wissenbach [b], Reinhart Poprawe [b]

[a] College of Materials Science and Technology, Nanjing University of Aeronautics and Astronautics, Yudao Street 29, 210016 Nanjing, People's Republic of China

[b] Fraunhofer Institute for Laser Technology ILT/Chair for Laser Technology LLT, RWTH Aachen, Steinbachstraße 15, D-52074 Aachen, Germany

Received 5 December 2011; received in revised form 5 February 2012; accepted 1 April 2012
Available online 1 May 2012

Abstract

This work presents a comprehensive study of the densification behavior, phase and microstructure development, hardness and wear performance of commercially pure Ti parts processed by selective laser melting (SLM). An in-depth relationship between SLM process, microstructures, properties, and metallurgical mechanisms has been established. A combination of a low scan speed and attendant high laser energy density resulted in the formation of microscopic balling phenomenon and interlayer thermal microcracks, caused by a low liquid viscosity, a long liquid lifetime, and resultant elevated thermal stress. In contrast, using a high scan speed produced the disorderly liquid solidification front and considerably large balling, due to an elevated instability of the liquid induced by Marangoni convection. A narrow, feasible process window was accordingly determined to eliminate process defects and result in full densification. The phase constitutions and microstructural characteristics of SLM-processed Ti parts experienced a successive change on increasing the applied scan speeds: relatively coarsened lath-shaped $\alpha \rightarrow$ refined acicular-shaped martensitic $\alpha' \rightarrow$ further refined zigzag-structured martensitic α', due to the elevated thermal and kinetic undercooling and attendant solidification rate. The optimally prepared fully dense Ti parts had a very high hardness of 3.89 GPa, a reduced coefficient of friction of 0.98 and wear rate of 8.43×10^{-4} mm^3 N^{-1} m^{-1} in dry sliding wear tests. The formation of an adherent, plastically smeared tribolayer on the worn surface contributed to the enhancement of wear performance.

Keywords: Selective laser melting (SLM); Laser treatment; Titanium; Wear; Microstructure

1. Introduction

Additive manufacturing (AM) technology has experienced more than 20 years of development and is presently a rapidly developing advanced manufacturing technique worldwide [1–4]. Unlike the material removal method in conventional machining processes, AM is based on a completely opposite philosophy, i.e. material incremental manufacturing. AM implies layer-by-layer shaping and consolidation of feedstock (typically powder materials) to a wide range of configurations, normally using a computer-controlled laser as the energy source [5–7]. First, a computer-aided design (CAD) model of the object to be built is mathematically sliced into thin layers. The object is then created by selective consolidation of the deposited material layers with a scanning laser beam. Each shaped layer represents a cross-section of the sliced CAD model. AM technology accordingly offers a wide range of advantages such as net-shape fabrication without the need of expensive moulds, direct production based on CAD models, high levels of process flexibility, and high material utilization rates [8–10]. The current development focus of AM technology is to produce complex shaped functional metallic components, including metals, alloys and metal matrix

* Corresponding author at: College of Materials Science and Technology, Nanjing University of Aeronautics and Astronautics, Yudao Street 29, 210016 Nanjing, People's Republic of China. Fax: +86 25 52112626.
E-mail address: dongdonggu@nuaa.edu.cn (D. Gu).

1359-6454/$36.00
http://dx.doi.org/10.1016/j.actamat.2012.04.006

composites (MMCs) [4], that cannot be easily produced by the conventional methods, in order to meet the demanding requirements of the aerospace [11], automotive [12], rapid tooling [13] and biomedical [14] sectors.

Direct metal laser sintering (DMLS) and selective laser melting (SLM), which are capable of processing a wide range of metals, alloys and MMCs, are presently regarded as the most versatile AM processes [15–18]. In general, DMLS is based on a liquid-phase sintering (LPS) mechanism involving a partial melting of the powder (i.e. semi-solid consolidation mechanism) [7,15]. SLM of metallic powder, however, is based on a complete melting/solidification mechanism [1,18]. The idea of full melting is supported by the continuously improved laser processing conditions in recent years, e.g., higher laser power, smaller focused spot size, thinner layer thickness, etc.

It should be noted that early attempts to process pure metals using DMLS proved to be unsuccessful, due to the considerably high viscosity and resultant balling phenomenon caused by the limited liquid formation [15,19]. The insufficient densification and heterogeneous microstructures and properties are regarded as major problems with DMLS-processed powder. Consequently, post-processing treatment such as furnace post-sintering [20], hot isostatic pressing (HIP) [11] or secondary infiltration with a low-melting-point material [21] is normally necessary to obtain the desired mechanical properties. The development of SLM has been driven by the demand to produce fully dense parts with mechanical properties comparable to those of bulk materials and by the desire to avoid time-consuming post-processing cycles. In contrast to DMLS, the density of SLM-processed pure metals can be improved significantly up to 99.5% through the full melting mechanism. More importantly, one of the major advances of SLM lies in the possibility it offers to process pure metals, e.g. Ti, Al, and Cu, which to date cannot be processed well with DMLS [1,4].

Nevertheless, SLM requires higher energy levels, which are normally achieved by applying a high laser power and using a thin powder layer thickness (i.e., long building time). SLM is therefore prone to suffer from instability of the molten pool due to the full melting mechanism used. A large degree of shrinkage tends to occur during liquid–solid transformation, accumulating considerable stresses in SLM-processed components. The complex residual stresses arising during cooling are regarded as key factors responsible for the distortion and even delamination of the final parts. In addition, the melt instability may result in spheroidization of the liquid within the molten pool (known as the "balling" effect [22]) and attendant interior porosity. Furthermore, SLM is characterized by extremely high temperature gradients and a rapid solidification nature, giving rise to the uncontrollable development of non-equilibrium phases and microstructures. The stability, configuration and thermal behavior of the molten pool during SLM may determine, to a great extent, the occurrence of the above problems [1,4]. Normally, the molten pool will exhibit multiple modes of heat and mass transfer, and in some instances, non-equilibrium phase transformations during SLM. Both SLM processing parameters (e.g. spot size, laser power, scan speed and layer thickness) and powder material properties (e.g. particle size and morphology, thermal conductivity and liquid surface tension) play a large role in determining the metallurgical nature of the pool and resultant microstructural and mechanical properties of SLM-processed powder.

Commercially pure (CP) Ti, due to its good biocompatibility and high mechanical strength, is typically used in laser-based AM processes to produce tailor-made implants for orthopedics and dentistry [23–26]. Load-bearing Ti implants, e.g. hip joint replacement implants, are often subject to wear in specific areas [27]. However, the relatively higher wear rate of traditional hip replacements is a cause of serious concern due to osteolysis and aseptic loosening [28], which is one of the major drawbacks limiting the life of hip replacements [27,28]. Tribological and wear properties, accordingly, determine some of the biomedical application capabilities of Ti implants. Nevertheless, to the best of the authors' knowledge, there are still no comprehensive previous studies focusing on the inherent relationship between the wear performance, constitution phases and microstructures of laser additive manufactured CP Ti which has wide potential applications in the biomedical industry.

In this work, SLM was applied to process CP Ti powder, which typically demonstrates a high tendency for balling effect and porosity formation when processed using DMLS [7]. The phase and microstructural developments at various SLM processing parameters were studied and the mechanical properties in terms of densification, hardness and wear resistance were assessed. The aim of this work is to establish a relationship between processing conditions, microstructural characteristics, and mechanical performance of CP Ti parts processed by SLM.

2. Experimental procedures

2.1. Powder material

CP Ti powder (ASTM Grade 2, supplied by TLS Technik GmbH, Germany) was used in this study; the chemical compositions are listed in Table 1. The Ti powder had a spherical shape (Fig. 1a) and particle size $d_{50} = 19.5$ μm and $d_{100} = 43.3$ μm (Fig. 1b).

2.2. SLM process

The SLM system, as schematically depicted in Fig. 2a, was developed by the Fraunhofer ILT and consisted

Table 1
Chemical compositions of as-used CP Ti powder.

Element	Ti	Fe	O	C	N	H
Content (wt.%)	Balance	0.03	0.19	0.02	0.04	0.005

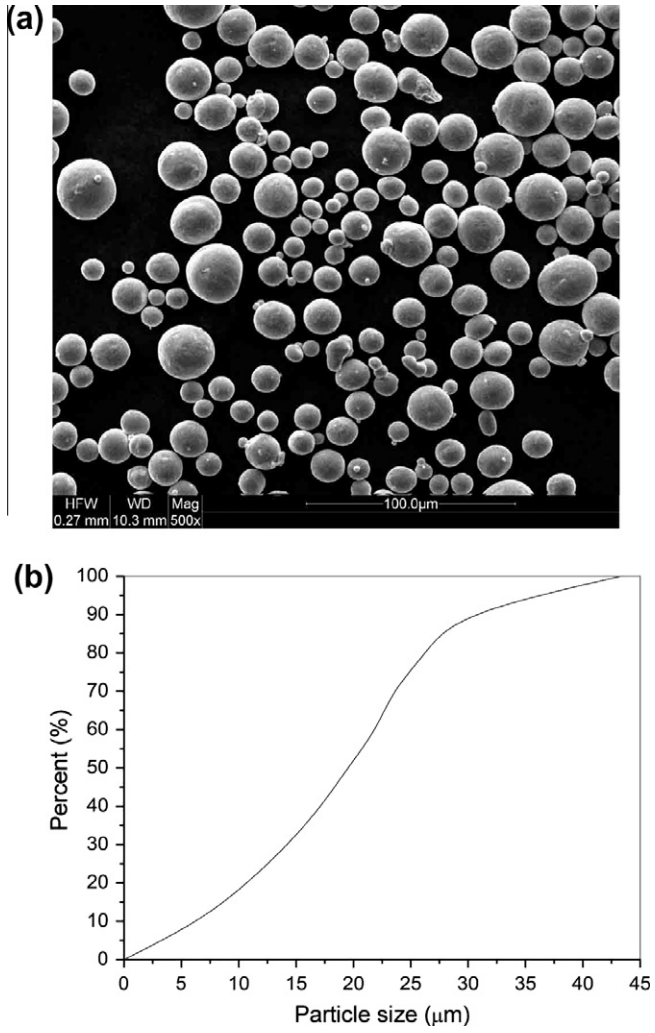

Fig. 1. (a) Particle morphology and (b) particle size distribution of the starting CP Ti powder.

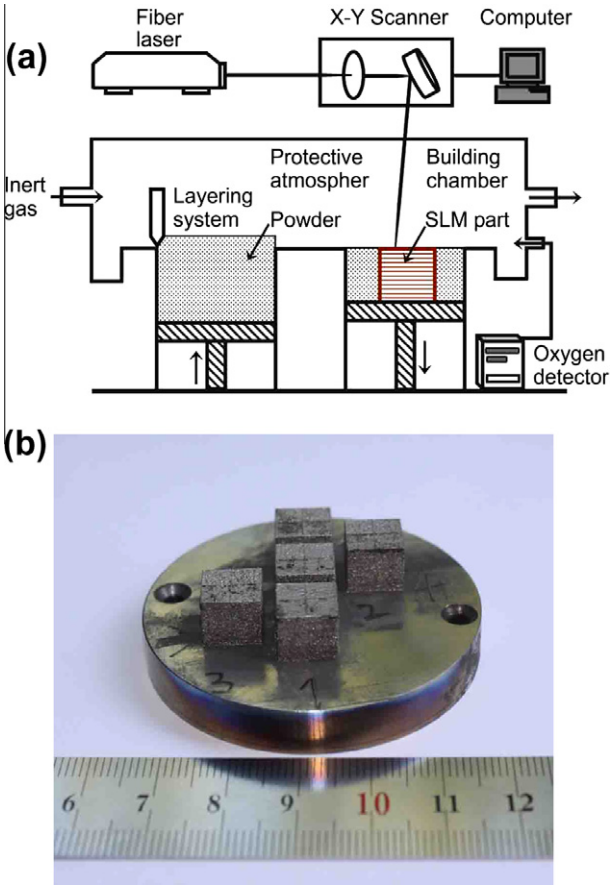

Fig. 2. (a) Schematic of SLM apparatus and (b) photograph of SLM-processed Ti parts.

mainly of a YLR-200 ytterbium fiber laser with a power of ~200 W and a spot size of 70 μm (IPG Laser GmbH, Germany), an automatic powder layering apparatus, an inert argon gas protection system, and a computer system for process control. When specimens were to be prepared, a Ti substrate was fixed on the building platform and leveled. Argon gas with an outlet pressure of 30 mbar was fed into the sealed building chamber and the resultant oxygen content decreased below 10 ppm. A thin layer of the powder, 50 μm thick, was then deposited on the substrate by the layering system. Afterwards, the laser beam scanned the powder bed surface to form a layerwise profile according to the CAD data of the specimens. Based on a series of preliminary experiments, the laser power (P) was optimized at 90 W. Meanwhile, the scan speeds (v) were set at 100, 200, 300 and 400 mm s^{-1} by the SLM control program, in order to change the processing conditions during one batch of experiment. Four different "linear energy densities" (LEDs) of 900, 450, 300, and 225 J m^{-1}, which were defined by [29]:

$$\text{LED} = \frac{\text{Laser power},P}{\text{Scan speed},v} \quad (1)$$

were used to assess the laser energy input to the powder layer being processed. A simple linear raster scan pattern was applied, using a scan vector length of 4 mm and a hatching spacing of 50 μm. The cubic specimens with dimensions of 8 mm × 8 mm × 8 mm were built in a layer-by-layer manner. The as-prepared CP Ti parts showed a good surface finish without macroscopic balling phenomenon and dimensional distortion (Fig. 2b).

2.3. Microstructural characterization

Phase identification was performed by X-ray diffraction (XRD) using a D8 Advance X-ray diffractometer (Bruker AXS GmbH, Germany) with Cu K_α radiation at 40 kV and 40 mA, using a continuous scan mode. A quick scan at 4° min^{-1} was first performed over a wide range of $2\theta = 30$–90° to give a general overview of the diffraction peaks. A slower scan rate of 1° min^{-1} was then used over $2\theta = 37.5$–39.5° and $2\theta = 39.5$–41.5° to obtain a more accurate determination of the diffraction peaks. Samples for metallographic examinations were cut, ground and polished according to standard procedures and etched with a

solution consisting of HF (2 ml), HNO_3 (4 ml) and distilled water (94 ml) for 30 s. Microstructures were characterized using a PMG3 optical microscopy (Olympus Corporation, Japan) and by a Quanta 200 scanning electron microscopy (SEM) (FEI Company, The Netherlands) in secondary electron mode at 20 kV.

2.4. Mechanical properties tests

The density (ρ) of SLM-processed specimens was determined based on the Archimedes principle. Nanoindentation tests on the polished sections of SLM parts were performed using a DUH-W201S nanoindentation tester (Shimadzu Corporation, Japan) at room temperature. A loading–unloading test mode was used and a test force 100 mN, a loading speed 1.3239 mN s^{-1} and a hold time 10 s were chosen. During measurements, the load and indentation depth were recorded. The raw data were then used to construct loading–unloading plots. The hardness was defined as a ratio of the peak indentation load (F_{max}) to the projected area of hardness impression (A_c). The Oliver–Pharr method [30] was applied to calculate the dynamic nanohardness (H_d):

$$H_d = \frac{F_{max}}{A_c} = \frac{F_{max}}{26.43h_c^2} \quad (2)$$

where h_c is the contact depth under the maximum indentation load. Dry sliding wear tests were conducted in a HT-500 ball-on-disk tribometer (LanZhou ZhongKe KaiHua Sci. & Technol. Co., Ltd., PR China) in air at room temperature. Surfaces of specimens were ground and polished prior to wear tests. A 3 mm diameter bearing steel GCr15 ball with a mean hardness of HRC60 was taken as the counterface material and a test load of 3 N was applied. The friction unit was rotated at a speed of 560 rpm for 30 min, with the rotation radius fixed at 2 mm. The coefficient of friction (COF) of the specimens was recorded during wear tests. The wear volume (V) was determined gravimetrically using:

$$V = M_{loss}/\rho \quad (3)$$

where M_{loss} was the weight loss of the specimens after wear tests. The wear rate (ω) was calculated by:

$$\omega = V/(WL) \quad (4)$$

where W was the contact load and L was the sliding distance.

3. Results and discussion

3.1. Phase identification

Typical XRD spectra of SLM-processed Ti parts obtained within a wide 2θ range (30–90°) are depicted in Fig. 3. Diffraction peaks corresponding to hexagonal close-packed (hcp) Ti (JCPDS Card No. 89-3725) were generally detected in SLM-processed samples using

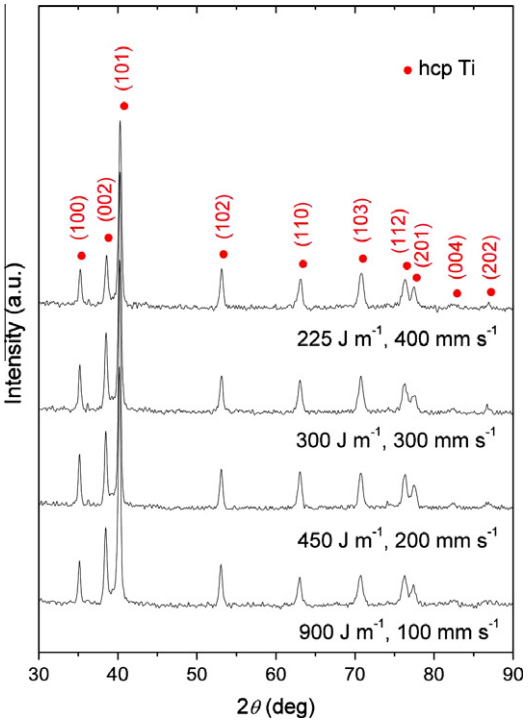

Fig. 3. XRD spectra of SLM-processed Ti parts at different processing parameters, obtained over a wide range of 2θ.

different processing parameters. The XRD characterization within small 2θ angles, as depicted in Fig. 4, revealed that the exact 2θ locations of the diffraction peaks for hcp Ti apparently changed with the applied SLM conditions. Here, the standard diffraction peaks for hcp Ti (α phase), located at $2\theta = 38.446°$ (~38.45°) and $2\theta = 40.177°$ (~40.18°), were taken for a comparison. At a relatively low v of 100 mm s^{-1} and attendant high LED of 900 J m^{-1}, the 2θ locations of the hcp Ti diffraction peaks of SLM-processed part were entirely the same as that of the standard α phase (Table 2). As the applied v increased above 200 mm s^{-1}, the 2θ locations of the diffraction peaks for hcp Ti generally shifted to higher 2θ (Fig. 4). These hcp Ti diffraction peaks corresponded to martensitic α' phase. A more significant shift of 2θ locations to larger values was detected on increasing the applied scan speeds (Table 2). When the highest v of 400 mm s^{-1} was used, the diffraction peaks for hcp α' phase became considerably broadened (Fig. 4) and the intensity showed a significant decrease (Table 2), which implied the formation of considerably refined crystals and microstructures in SLM-processed Ti in this instance.

Theoretically, pure Ti exhibits an allotropic phase transformation at 882 °C, changing from body-centered cubic (bcc) crystal structure (β phase) at higher temperatures to hcp crystal structure (α phase) at lower temperatures [31]. SLM of Ti proceeds via a complete melting and solidification mechanism. The solidification behaviors of the molten pool with complete liquid formation, including thermal history, liquid flow and solidification rate, determine the

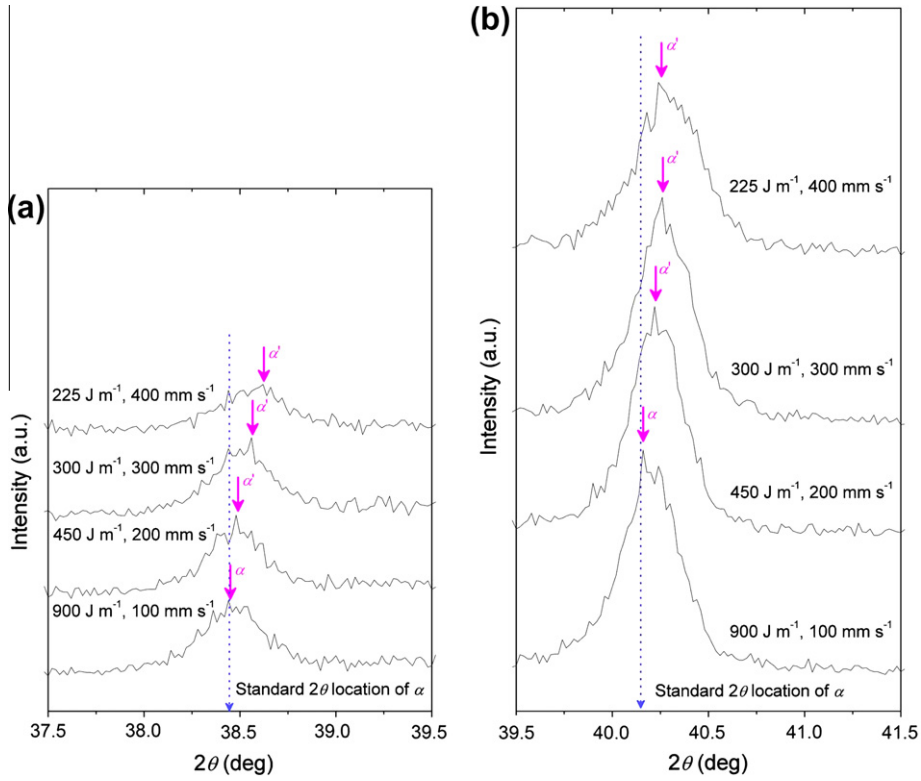

Fig. 4. XRD spectra in the vicinity of the standard diffraction peaks of hcp Ti phase (a) $2\theta = 38.45°$ and (b) $2\theta = 40.18°$, showing the variation of constitution phase in SLM-processed Ti parts at different processing parameters.

Table 2
XRD data showing the displacement and intensity variation of identified peaks for hcp Ti phase.

Sample	2θ location (°)	Intensity (CPS)	2θ location (°)	Intensity (CPS)
Standard (PDF No. 89-3725)	38.45		40.18	
900 J m^{-1}, 100 mm s^{-1}	38.45	614.91	40.18	1719.7
450 J m^{-1}, 200 mm s^{-1}	38.48	619.91	40.22	1659.8
300 J m^{-1}, 300 mm s^{-1}	38.56	689.90	40.26	1814.7
225 J m^{-1}, 400 mm s^{-1}	38.62	394.94	40.24	1204.8

phase transformation in the finally solidified materials. As a general rule, laser melting offers high heating/cooling rates (10^3–10^8 K s^{-1}) leading to the possibility of developing non-equilibrium phases [32]. In the present study, it is found that the phase formation in SLM-processed Ti is determined by the applied laser scan speed and LED, i.e.

(i) $\beta \rightarrow \alpha$ ($v = 100$ mm s^{-1});
(ii) $\beta \rightarrow$ martensitic α' ($v \geqslant 200$ mm s^{-1}).

Essentially, the laser scan speed influences the phase transformation by changing the operative undercooling degree and solidification rate. In the laser solidification process, the local growth velocity of solidification front, v_s, can be calculated directly by measuring the angle (θ) between v_s and laser scan speed v [33]:

$$v_s = v\cos\theta \tag{5}$$

The thermal undercooling and kinetic undercooling within the pool can be expressed respectively as follows [34]:

$$\Delta T_t = \frac{\Delta H_f}{c_p^l} F_{Iv}(P_t) \tag{6.1}$$

$$P_t = \frac{v_s R}{2D_T} \tag{6.2}$$

where ΔH_f is the heat of fusion (J mol^{-1}), c_p^l is the specific heat of the liquid (J mol^{-1} K^{-1}), F_{Iv} is the Ivantsov function, P_t is the thermal Péclet number, R is the curvature radius of the crystal tip (m), and D_T is the thermal diffusivity (m^2 s^{-1}).

$$\Delta T_k = \frac{v_s}{\lambda} \tag{7.1}$$

$$\lambda = \frac{\Delta H_f v_0}{k_B T_L^2} \tag{7.2}$$

where λ is the interfacial kinetic coefficient, v_0 is the speed of sound (m s^{-1}), k_B is the Boltzmann constant, and T_L is the liquidus temperature (K). At a low v, the input LED during line-by-line scanning is relatively high, leading to an elevated thermalization of the energy and attendant

higher SLM temperature. Due to a significant thermal accumulation within the molten pool, the effect of quenching that occurs by conduction of heat through the substrate is not significant in this situation, favoring the complete transformation of $\beta \rightarrow \alpha$ phase after solidification. On increasing the applied laser scan speed, the solidification rate of the liquid front within the pool increases (Eq. (5)), thereby enhancing both thermal undercooling (Eq. (6)) and kinetic undercooling (Eq. (7)). The significantly enhanced temperature gradients within the pool result in martensitic transformation, leading to the formation of α' phase in the finally solidified Ti parts (Fig. 4). According to Bragg's law [35]

$$2d \sin\theta = n\lambda (n = 1, 2, 3, \ldots) \tag{8}$$

the observed increase of 2θ at a higher scan speed (Fig. 4 and Table 2) indicates a decrease in the lattice plane distance d, which is believed to be caused by the prevailing martensitic transformation. Normally, the occurrence of martensitic transformation is accompanied by microscopic volume expansion, which in turn creates stresses at grain boundaries that may influence the lattice parameters [36].

3.2. Surface morphology

Fig. 5 illustrates the characteristic surface morphologies of SLM-processed Ti parts observed at a relatively low magnification. The surfaces of Ti parts processed at scan speeds of 100–300 mm s^{-1} were completely dense, showing no apparent pores or cracks. Continuous scan tracks with sound intertrack bonding were generally formed. Small-sized metallic balls with diameter of tens of micrometers ("balling" effect) were occasionally observed on the surfaces (Fig. 5a–c). At an even higher v of 400 mm s^{-1}, although the surface was almost fully dense, several clusters of microsized balls were formed on the surface, increasing its roughness significantly (Fig. 5d).

Surface observation at a higher magnification, as shown in Fig. 6, revealed some interesting variations in solidification features (e.g. liquid flow and balling initiation behaviors) at different SLM parameters. At a relatively low v of 100 mm s^{-1} and resultant high LED of 900 J m^{-1}, a large amount of considerably small-sized balls with diameters below 10 μm were formed along the solidified liquid front (Fig. 6a), implying the occurrence of balling effect at a microscopic scale. Interestingly, at a reasonable v of 200 mm s^{-1}, a clear and regular liquid solidification front free of any balling phenomenon was observed, yielding stable and continuous scan tracks (Fig. 6b). On increasing v to 300 mm s^{-1}, however, the liquid solidification front started to become irregular and, meanwhile, a small number of balls were present (Fig. 6c). At an even higher v of 400 mm s^{-1}, the liquid solidification front became considerably disorderly, producing interrupted scan tracks and large-sized balls on the tracks (Fig. 6d). A close examination of Figs. 5 and 6, accordingly, revealed the following two aspects of problems under the extreme SLM conditions:

(i) too low v and too high LED resulted in microscopic balling phenomenon (Fig. 6a);
(ii) too high v resulted in turbulent liquid solidification front and significant balling occurrence (Figs. 5d and 6d).

During SLM, the dynamic viscosity μ of a molten pool consisting entirely of Ti liquid is dependent on temperature T and can be assessed by [37]:

$$\mu = \frac{16}{15}\sqrt{\frac{m}{k_B T}}\gamma \tag{9}$$

where m is the atomic mass and γ is the surface tension of Ti liquid. Using a lower v leads to a longer dwelling time of the beam on the surface of molten pool and attendant higher LED input to the pool, thereby enhancing the operative T significantly. The dynamic viscosity of the Ti liquid within the pool accordingly decreases. The combined influence of a long liquid lifetime and a low viscosity results in a high degree of overheating of the liquid and attendant elevated melt instability. A number of small-sized liquid droplets tend to splash from the liquid front being solidified, due to the reduction in the surface energy of liquid at short length scales (Fig. 6a).

On the other hand, as revealed in Eqs. (6) and (7), when localized powder melting occurs during laser scanning, significant temperature gradients will be formed within the molten pool. The temperature gradients in the pool give rise to surface tension gradients and resultant Marangoni convection. The formation of such convective streams within the pool tends to increase the magnitude of the thermocapillary force and resultant instability of the liquid [38]. The higher the applied scan speed, the more significant the Marangoni convection and liquid capillary instability effect will be. The liquid surface flow, consequently, occurs from a region of low surface tension to a region of high surface tension, changing the direction of liquid flow from radially outward to inward [39]. The radially inward flow causes the liquid to spheroidize towards the laser beam center and increases the tendency for the formation of relatively coarsened balls (Figs. 5d and 6d). In this situation, the advancing liquid solidification front is significantly disturbed due to the presence of large balls and, thus, becomes interrupted after solidification (Fig. 6d).

3.3. Densification behavior

The cross-section microstructures of Ti parts processed using various SLM parameters are provided in Fig. 7. Layerwise microstructural features were generally observed, due to the layer-by-layer incremental deposition manner of the SLM process. Nevertheless, the microstructures on cross-sections, e.g. the configuration of the solidified molten pool, residual porosity and layer distribution state, were found to be dependent on the SLM conditions used. At a relatively low v of 100 mm s^{-1} and a high LED of 900 J m^{-1}, thin, narrow microcracks with an average

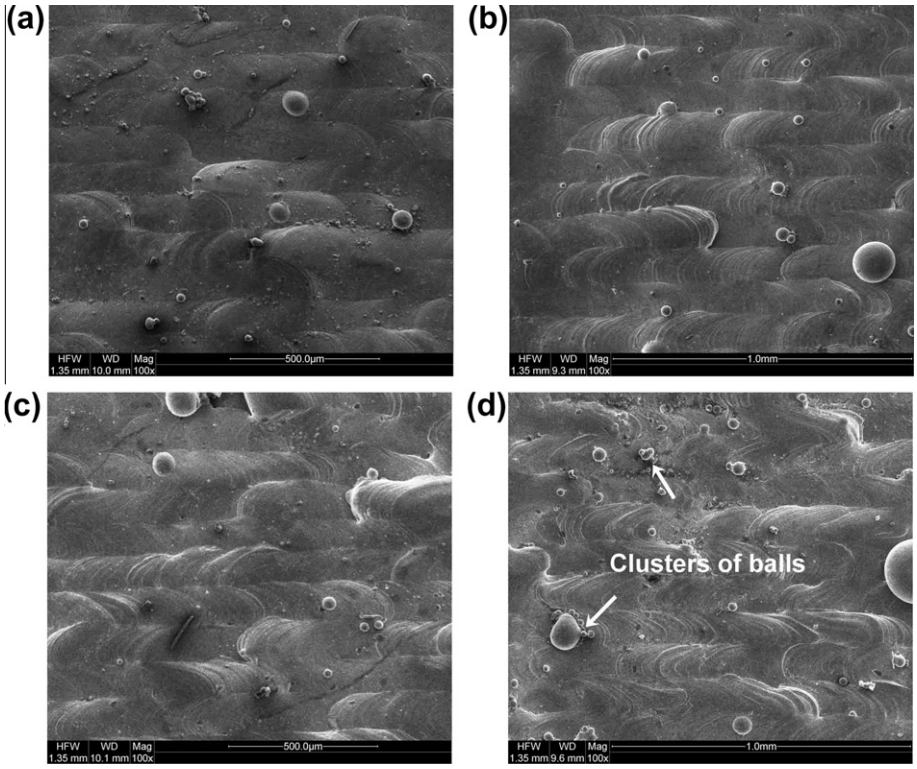

Fig. 5. SEM images showing typical surface morphologies of SLM-processed Ti parts using various processing parameters: (a) 900 J m^{-1}, 100 mm s^{-1}; (b) 450 J m^{-1}, 200 mm s^{-1}; (c) 300 J m^{-1}, 300 mm s^{-1}; (d) 225 J m^{-1}, 400 mm s^{-1}.

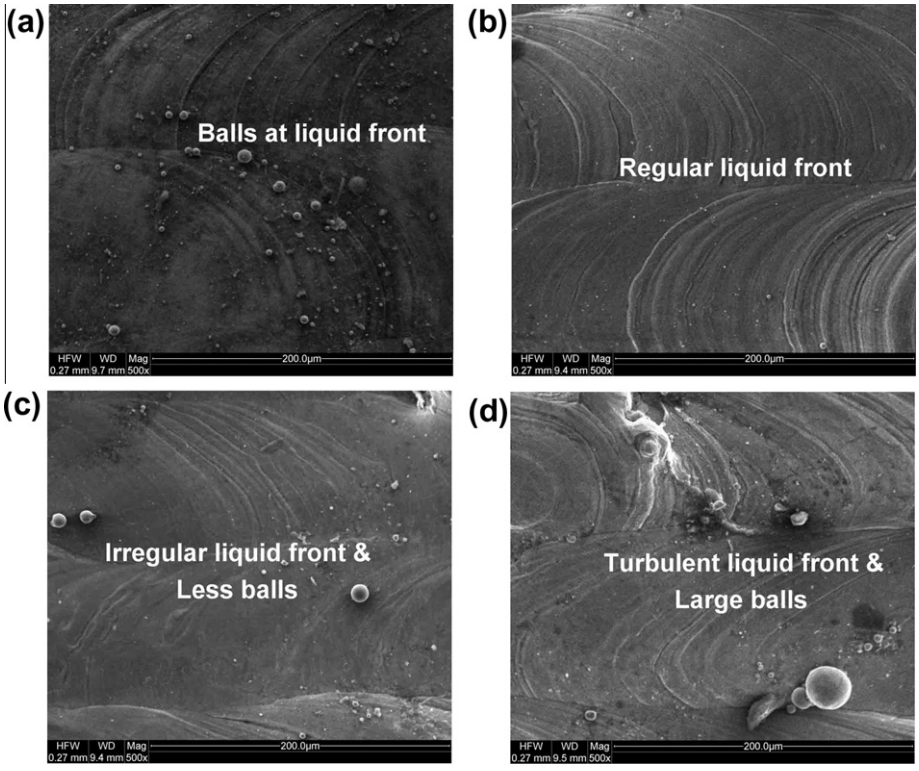

Fig. 6. SEM images showing liquid flow characteristics on the corresponding surfaces in Fig. 5a (a), Fig. 5b (b), Fig. 5c (c), and Fig. 5d (d).

length of ~400 μm were present between the neighboring layers (Fig. 7a), producing 3.3% porosity in the SLM part. Dense, metallurgically bonded layers without any inter-layer pores or cracks were formed as the v increased to

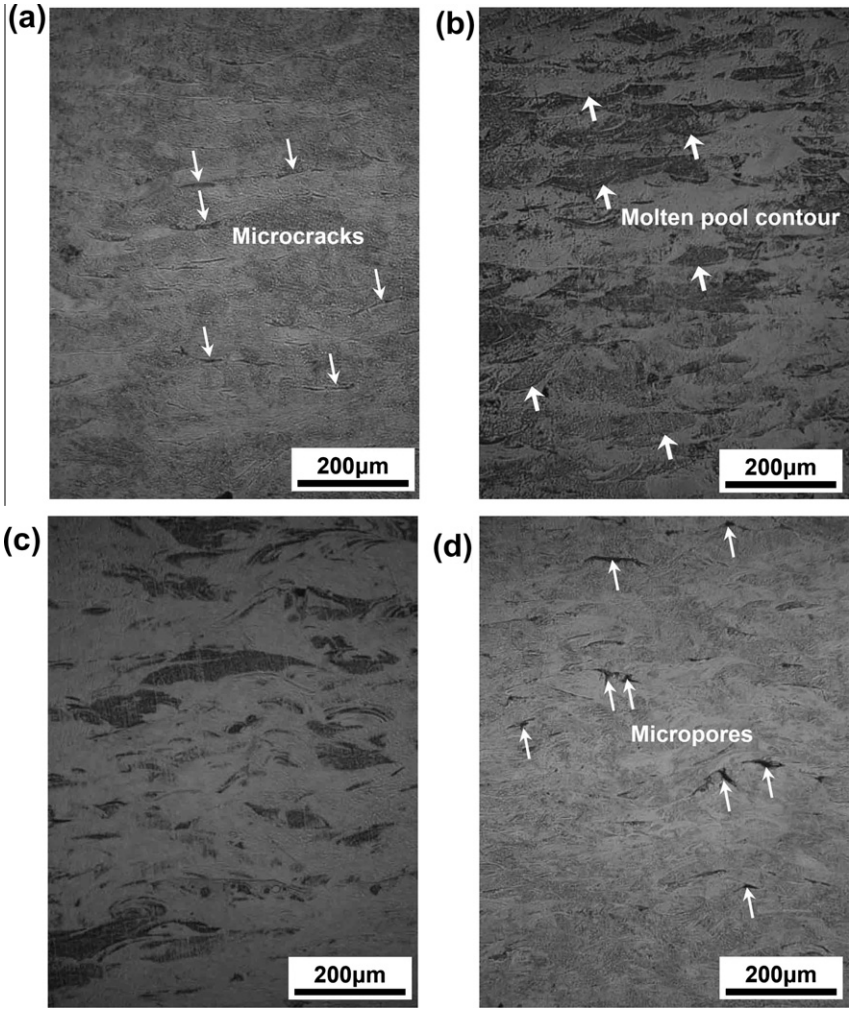

Fig. 7. Optical microscopy images showing interlayer microstructures on cross-sections of SLM-processed Ti parts at different processing parameters: (a) 900 J m^{-1}, 100 mm s^{-1}; (b) 450 J m^{-1}, 200 mm s^{-1}; (c) 300 J m^{-1}, 300 mm s^{-1}; (d) 225 J m^{-1}, 400 mm s^{-1}.

200 mm s^{-1}. The as-solidified molten pools generally had a clear configuration, typically showing a stable solidification front (Fig. 7b). At a higher v of 300 mm s^{-1}, although the cross-section microstructure of SLM part was still fully dense, the distribution state of the layers became uneven. The structures of solidified molten pools were elongated along the laser scan direction (Fig. 7c), implying a significantly elevated thermodynamics of the pool as the scan speed increased. In these two instances, the obtainable densification rate of SLM parts generally approached 99.5%. At an even higher v of 400 mm s^{-1} and attendant low LED of 225 J m^{-1}, irregularly shaped micropores with a mean size of ~30 μm were formed in the interlayer areas (Fig. 7d), thereby increasing the residual porosity of the SLM part to 5.7%.

The microcracks formed at a low v and attendant high LED (Fig. 7a) are believed to be thermal cracks caused by residual thermal stresses. During the SLM densification process, shrinkage occurs rapidly once the powder material becomes fully molten. A nominally flat powder bed surface becomes a curved surface or a recessed region due to the effect of densification caused by conversion of loose powder to dense liquid [40]. The shrinkage and resultant development of residual stresses during SLM have been studied using finite-element modeling (FEM) by Dai and Shaw [41] and an analytical solution has been given by Xiao and Zhang [42]. The dominant mechanism inducing residual stresses in a SLM part is the tendency of the cool-down phase of the molten top layer to shrink due to the thermal contraction; meanwhile, however, such a deformation is inhibited by the underlying previously processed layers. Zhu et al.'s study on the shrinkage behavior of metallic powder during laser melting [43] reveals that the thermal shrinkage for a chosen material increases as the input laser power P increases or the scan speed v decreases, i.e. as the operative LED increases (Eq. (1)). Consequently, considerable thermal stresses tend to generate and accumulate in the SLM part being solidified. The microcracks as illustrated in Fig. 7a are typically caused by hot cracking. Their formation is ascribed to the interruption of liquid film at grain boundaries in the solidification temperature range, due to the action of the tensile stresses [44]. Theoretical

and experimental studies by Mercelis and Kruth [45] have revealed that, in general, the residual stress profile in a SLM part consists of two zones of large tensile stresses at the top and bottom of the part, and a large zone of intermediate compressive stress in between. Therefore, the microcracks resulting from tensile stress (Fig. 7a) are typically located between two neighboring layers (i.e. on the top or bottom of two individual layers).

On the other hand, the formation of micropores at a high v (Fig. 7d) is ascribed to the occurrence of the balling phenomenon (Fig. 5d). The balling effect results in the formation of discontinuous scan tracks and interball porosity as a current layer is processed. Furthermore, during the layer-by-layer SLM process, the balling effect is a severe impediment to a uniform deposition of the fresh powder on the previously processed layer. During laser melting of such an uneven powder layer, especially as a high scan speed is applied, the movement front of the molten pool and the melt inside undergoes a significant disturbance and even interruption. Consequently, it is difficult to fill completely the interball pores on the surface of the previous layer with the melt, hence causing interlayer pores and a limited densification response (Fig. 7d).

3.4. Microstructural evolution

The characteristic crystalline structures of SLM-processed Ti parts developed under various processing conditions are shown in Fig. 8. At a relatively low v and resultant high LED, relatively coarse lath-shaped grains were present (Fig. 8a), which were identified as α phase by XRD (Fig. 4). As the v increased to 200 mm s^{-1}, the martensitic transformation occurred (Fig. 4) and the formed α' phase changed into a relatively refined acicular shape (Fig. 8b). At an even higher $v \geqslant 300$ mm s^{-1}, the crystalline structures of martensitic α' phase were further refined, changing into a zigzag form with a size <10 μm (Fig. 8c and d). The significant grain refinement of α' phase at 400 mm s^{-1} and 225 J m^{-1} was also confirmed by the presence of the considerably broadened α' diffraction peaks with a low intensity in the XRD analysis (Fig. 4 and Table 2). Therefore, combined with the phase and microstructure studies (Figs. 4 and 8), the XRD and optical microscopy analysis revealed that on increasing the laser scan speed and attendant undercooling degree and solidification rate (Eqs. (5)–(7)), the microstructural features of SLM-processed Ti experienced an interesting change as follows: relatively coarsened lath-shaped $\alpha \rightarrow$ refined acicular-shaped $\alpha' \rightarrow$ further refined zigzag-structured α'.

3.5. Hardness and wear performance

Fig. 9a depicts the nanoindentation load–depth curves measured on the polished sections of SLM-processed Ti parts. The indentation depths of the parts processed at a low v of 100 mm s^{-1} (1.2762 μm) and a high v of 400 mm s^{-1} (1.1389 μm) were larger than those of the parts prepared using the optimal scan speeds (1.0168 μm at 200 mm s^{-1} and 0.9869 μm at 300 mm s^{-1}). The corresponding dynamic nanohardness H_d values (2.32 GPa at 100 mm s^{-1} and 2.92 GPa at 400 mm s^{-1}) were considerably lower than those obtained at scan speeds of 200 mm s^{-1} (3.66 GPa) and 300 mm s^{-1} (3.89 GPa), as revealed in Fig. 9b. Nevertheless, the SLM-processed Ti parts, for all the given processing parameters, demonstrated superior hardness property compared to conventional powder metallurgy (PM) processed Ti with a typical hardness of ~1 GPa [46]. In general, residual

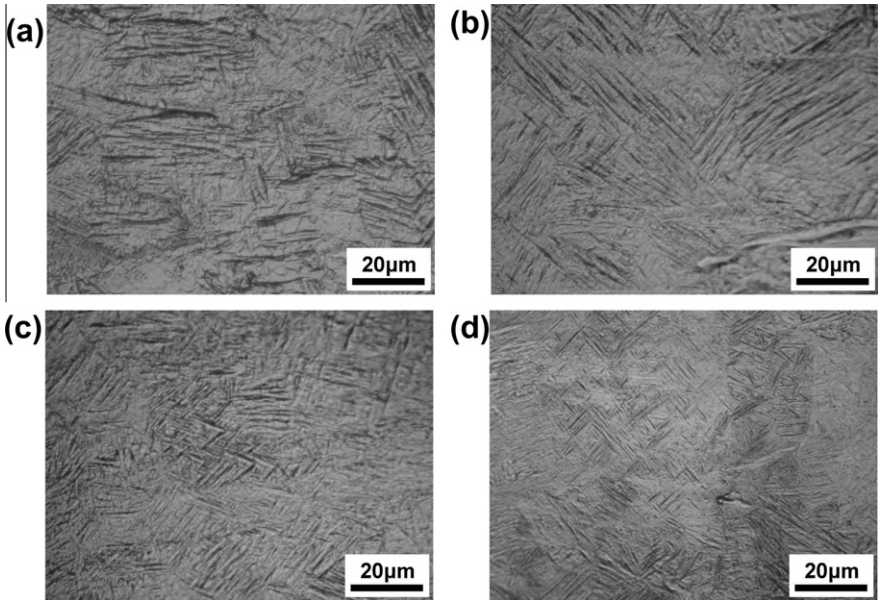

Fig. 8. Optical microscopy images showing characteristic microstructures of SLM-processed Ti parts at different processing parameters: (a) 900 J m^{-1}, 100 mm s^{-1}; (b) 450 J m^{-1}, 200 mm s^{-1}; (c) 300 J m^{-1}, 300 mm s^{-1}; (d) 225 J m^{-1}, 400 mm s^{-1}.

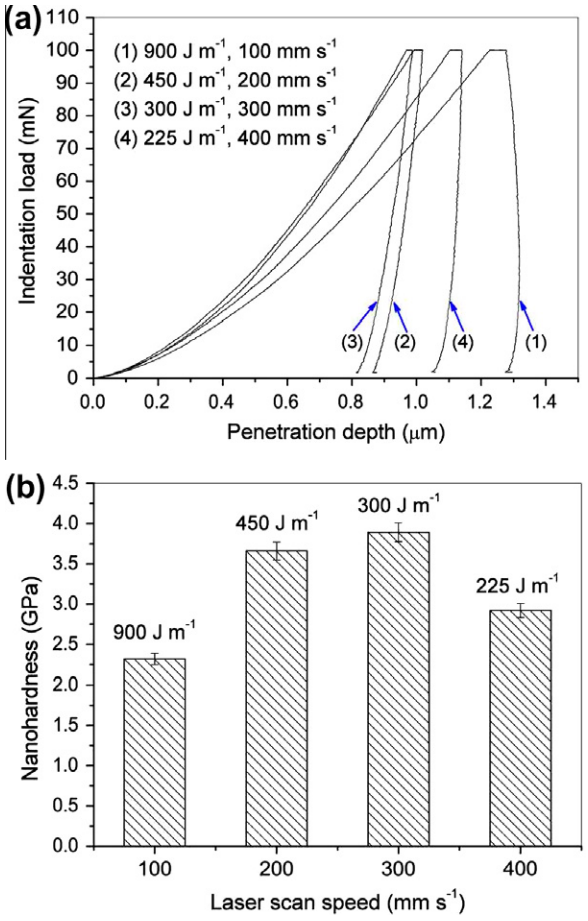

Fig. 9. (a) Loading–unloading curves and (b) calculated nanohardness obtained by nanoindentation tests on Ti parts processed using various SLM parameters.

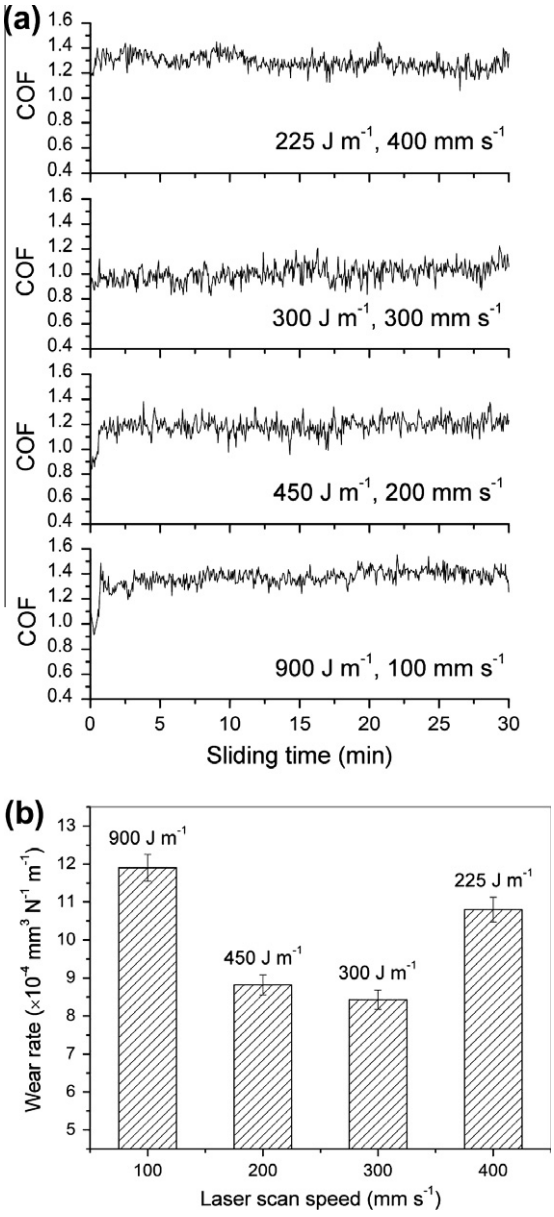

Fig. 10. (a) COF and (b) wear rate of SLM-processed Ti parts under different processing conditions.

stresses are quite large in layer-by-layer fabricated SLM parts, but residual stresses are not always disadvantageous [45]. On the premise of a sufficiently high densification without the formation of cracks or pores (Fig. 7b and c), the retention of a reasonable level of residual stress in SLM-processed parts favors the enhancement of hardness [47]. Moreover, the significant grain refinement effect (Fig. 8c) due to laser rapid solidification favors a further increase in the obtainable hardness.

Fig. 10 depicts the variations of COF and wear rate with sliding time for all four SLM-processed Ti samples. Detailed SEM studies of the corresponding worn surfaces are shown in Fig. 11 and the underlying mechanisms for the formation of various topographical features were proposed to be as follows. In general, the COF values for each specimen exhibited a relatively steady-state behavior with few local fluctuations. Nevertheless, the applied SLM conditions for various Ti samples exerted a significant influence upon the obtainable wear performance. At a relatively low v of 100 mm s^{-1}, the average COF reached a high value of 1.41 (Fig. 10a), resulting in a considerably elevated wear rate of 1.19×10^{-3} mm^3 N^{-1} m^{-1} (Fig. 10b). The worn surface primarily consisted of parallel, deep grooves representing abrasion wear. The presence of loose fragments at the edges of grooves revealed the local severe deformation and plowing of the surface during sliding. Some irregular shaped debris in the form of particles was also observed on the wear surface (Fig. 11a). On increasing v to 200 mm s^{-1}, the worn surface showed much shallower grooves, free of any loose abrasive fragments (Fig. 11b), thereby reducing the mean COF and attendant wear rate to 1.16 and 8.82×10^{-4} mm^3 N^{-1} m^{-1}, respectively (Fig. 10). Interestingly, using a reasonable v of 300 mm s^{-1}, the worn surface of Ti sample became rather smooth and was found to be covered with adhesion tribolayer (Fig. 11c). The lowest COF of 0.98 and wear rate of 8.43×10^{-4} mm^3 N^{-1} m^{-1} were accordingly obtained (Fig. 10). In this situation, due to the full densification response (Fig. 7c), the formation of refined α' martensitic

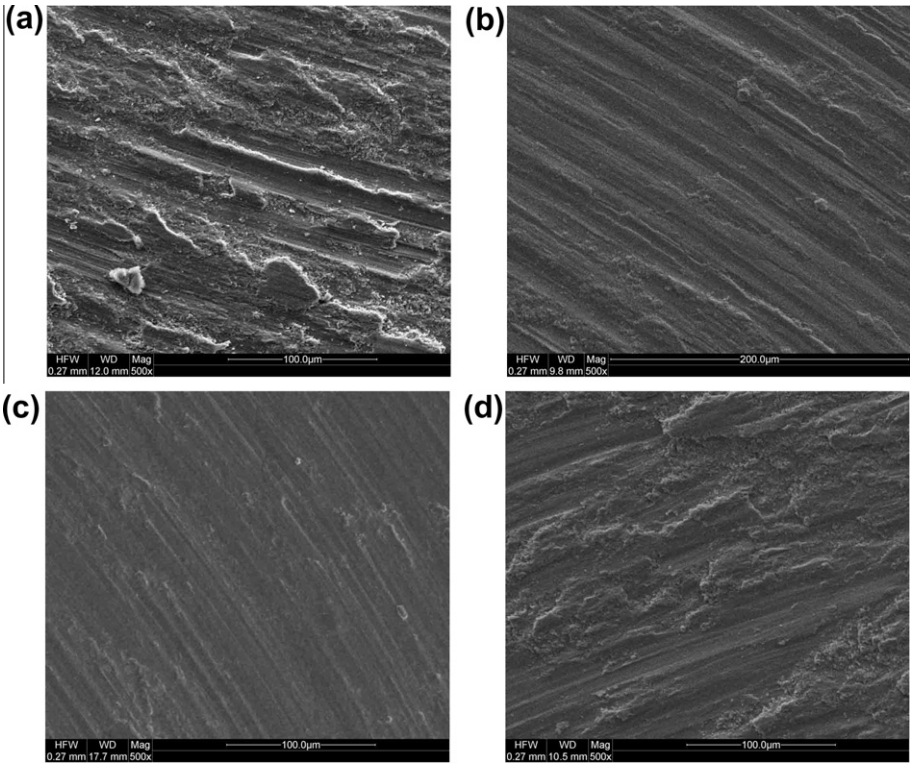

Fig. 11. SEM images showing characteristic morphologies of worn surfaces of SLM-processed Ti parts at: (a) 900 J m^{-1}, 100 mm s^{-1}; (b) 450 J m^{-1}, 200 mm s^{-1}; (c) 300 J m^{-1}, 300 mm s^{-1}; (d) 225 J m^{-1}, 400 mm s^{-1}.

microstructure (Fig. 8c), and the enhancement of hardness (Fig. 9), the protective tribolayer can easily smear plastically on the surface being slid [48]. It is thus reasonable to consider that the mechanism of material removal during sliding changes from abrasion (Fig. 11a) to adhesion of the tribolayer (Fig. 11c). Such a transition favors the reduction in wear rate after sliding. For SLM Ti sample processed at an even higher v of 400 mm s^{-1}, although the localized formation of tribolayer was still observed on the worn surface, severe spalling and delamination of the tribolayer occurred (Fig. 11d). The obtained COF value 1.29 and wear rate 1.08×10^{-3} mm^3 N^{-1} m^{-1} showed a significant increase in this case (Fig. 10).

A close comparison of the phase constitutions (Fig. 4), densification response (Fig. 7) and microstructural features (Fig. 8) of SLM-processed Ti parts reveals that the limited hardness and wear performance of the part processed at a low scan speed and a high LED is ascribed to: (i) the insufficient densification rate due to the formation of thermal microcracks (Fig. 7a); and (ii) the formation of relatively coarsened grains (Fig. 8a). For an SLM part processed at a high scan speed, although the formation of considerably refined martensitic α' phase (Fig. 8d) should favor the improvement in hardness and wear property, the limited densification behavior of the powder due to the presence of interlayer micropores (Fig. 7d) weakens the ultimate performance of the as-processed Ti part.

4. Conclusions

(1) The densification activity of SLM-processed CP Ti parts was controlled by the applied scan speed v and attendant LED. A combination of low v of 100 mm s^{-1} and high LED of 900 J m^{-1} resulted in microscopic balling phenomenon and interlayer thermal cracks, due to a low liquid viscosity, a long liquid lifetime and resultant elevated thermal stresses. Using a high v 400 mm s^{-1} produced a disorderly liquid solidification front and a significant balling effect, due to an enhanced instability of the liquid caused by Marangoni convection. Both defects, which were caused by inaccurate laser process control, lowered the densification rate. The fully dense Ti parts were achieved when a suitable process window (v of 200 and 300 mm s^{-1}, LED of 450 and 300 J m^{-1}) was properly determined.

(2) The phase constitutions and microstructural features of SLM-processed Ti parts experienced a successive change: relatively coarsened lath-shaped $\alpha \rightarrow$ refined acicular-shaped martensitic $\alpha' \rightarrow$ further refined zig-zag-structured martensitic α', as the applied laser scan speed increased, due to the elevated thermal and kinetic undercooling and attendant solidification rate.

(3) Both the insufficient densification caused by thermal microcracks (100 mm s^{-1}) and interlayer micropores (400 mm s^{-1}) and the formation of relatively coarsened α grains (100 mm s^{-1}) resulted in limited hardness and wear performance. The optimally prepared Ti parts (300 mm s^{-1} and 300 J m^{-1}) had a very high hardness of 3.89 GPa and a reduced COF of 0.98 and wear rate of 8.43×10^{-4} mm^3 N^{-1} m^{-1}. The formation of an adherent, plastically smeared tribolayer on the worn surface improved the wear performance.

Acknowledgments

Financial supports from the National Natural Science Foundation of China (Nos. 51104090 and 51054001), the Aeronautical Science Foundation of China (No. 2010ZE52053), the Natural Science Foundation of Jiangsu Province (No. BK2009374), and the Alexander von Humboldt Foundation are appreciated.

References

[1] Kruth JP, Levy G, Klocke F, Childs THC. CIRP Ann 2007;56:730–59.
[2] Bourell D, Wohlert M, Harlan N, Das S, Beaman J. Adv Eng Mater 2002;4:663–9.
[3] Mazumder J, Dutta D, Kikuchi N, Ghosh A. Opt Laser Eng 2000;34:397–414.
[4] Gu DD, Meiners W, Wissenbach K, Poprawe R. Int Mater Rev 2012;57:133–64.
[5] Sercombe TB, Schaffer GB. Acta Mater 2004;52:3019–25.
[6] Yu P, Schaffer GB. Acta Mater 2009;57:163–70.
[7] Fischer P, Romano V, Weber HP, Karapatis NP, Boillat E, Glardon R. Acta Mater 2003;51:1651–62.
[8] Yadroitsev I, Thivillon L, Bertrand Ph, Smurov I. Appl Surf Sci 2007;254:980–3.
[9] Fox P, Pogson S, Sutcliffe CJ, Jones E. Surf Coat Technol 2008;202:5001–7.
[10] Mumtaz KA, Erasenthiran P, Hopkinson N. J Mater Process Technol 2008;195:77–87.
[11] Das S, Wohlert M, Beaman JJ, Bourell DL. Mater Des 1999;20:115–21.
[12] Mazumder J, Schifferer A, Choi J. Mater Res Innovat 1999;3:118–31.
[13] Levy GN, Schindel R, Kruth JP. CIRP Ann 2003;52:589–609.
[14] Zhang LC, Klemm D, Eckert J, Hao YL, Sercombe TB. Scripta Mater 2011;65:21–4.
[15] Agarwala M, Bourell D, Beaman J, Marcus H, Barlow J. Rapid Prototyping J 1995;1(1):26–36.
[16] Gu DD, Shen YF. Metall Mater Trans B 2006;37:967–77.
[17] Roberts AP, Grayson G, Challis VJ, Zhang LC, Grotowski JF, Schaffer GB, et al. Acta Mater 2011;59:5257–65.
[18] Thijs L, Verhaeghe F, Craeghs T, Van Humbeeck J, Kruth JP. Acta Mater 2010;58:3303–12.
[19] Simchi A, Petzoldt F, Pohl H. Int J Powder Metall 2001;37:49–61.
[20] Agarwala M, Bourell D, Beaman J, Marcus H, Barlow J. Rapid Prototyping J 1995;1(2):36–44.
[21] Kumar S, Kruth JP. Mater Des 2007;28:400–7.
[22] Tolochko NK, Mozzharov SE, Yadroitsev IA, Laoui T, Froyen L, Titov VI, et al. Rapid Prototyping J 2004;10(2):78–87.
[23] Pattanayak DK, Fukuda A, Matsushita T, Takemoto M, Fujibayashi S, Sasaki K, et al. Acta Biomater 2011;7:1398–406.
[24] Fukuda A, Takemoto M, Saito T, Fujibayashi S, Neo M, Pattanayak DK, et al. Acta Biomater 2011;7:2327–36.
[25] Xue WC, Krishna BV, Bandyopadhyay A, Bose S. Acta Biomater 2007;3:1007–18.
[26] Jauer L, Meiners W. Manufacturing individual titanium implants using selective laser melting, annual report. Fraunhofer Institute for Laser Technology, Aachen, Germany; 2010. <http://www.ilt.fraunhofer.de/en/publication-and-press/annual-report/2010/annual-report-2010-p111.html>.
[27] Krishna BV, Xue WC, Bose S, Bandyopadhyay A. JOM 2008;60:45–8.
[28] Willert HG, Bertram H, Hans Buchhorn G. Clin Orthop Relat Res 1990;258:95–107.
[29] Gu DD, Shen YF. J Alloys Compd 2009;473:107–15.
[30] Oliver WC, Pharr GM. J Mater Res 1992;7:1564–83.
[31] Lütjering G, Williams JC. Titanium. 2nd ed. Berlin: Springer Verlag; 2007.
[32] Das M, Balla VK, Basu D, Bose S, Bandyopadhyay A. Scripta Mater 2010;63:438–41.
[33] Liu YC, Lan F, Yang GC, Zhou YH. J Cryst Growth 2004;271:313–8.
[34] Schwarz M, Arnold CB, Aziz MJ, Herlach DM. Mater Sci Eng A 1997;226–228:420–4.
[35] Zhou Y, Wu GH. Analysis methods in materials science—X-ray diffraction and electron microscopy in materials science. 2nd ed. Harbin: Harbin Institute of Technology Press; 2007.
[36] Moyer JM, Ansell GS. Metall Trans A 1975;6:1785–91.
[37] Takamichi I, Roderick ILG. The physical properties of liquid metals. Oxford: Clarendon Press; 1993.
[38] Simchi A, Pohl H. Mater Sci Eng A 2003;359:119–28.
[39] Niu HJ, Chang ITH. Scripta Mater 1999;41:1229–34.
[40] Dai K, Shaw L. Acta Mater 2005;53:4743–54.
[41] Dai K, Shaw L. Acta Mater 2001;49:4171–81.
[42] Xiao B, Zhang YW. Int J Heat Mass Transfer 2007;50:2161–9.
[43] Zhu HH, Lu L, Fuh JYH. Proc Inst Mech Eng B 2006;220:183–90.
[44] Zhong ML, Sun HQ, Liu WJ, Zhu XF, He JJ. Scripta Mater 2005;53:159–64.
[45] Mercelis P, Kruth JP. Rapid Prototyping J 2006;12(5):254–65.
[46] Matucha KH. Structure and properties of nonferrous alloys. Weinheim: VCH; 1996.
[47] Gu DD, Meiners W. Mater Sci Eng A 2010;527:7585–92.
[48] Jain A, Basu B, Kumar BVM, Harshavardhan, Sarkar J. Acta Mater 2010;58:2313–23.